Systematic investigation of localized surface plasmon resonance of long-range ordered Au nanodisk arrays

Yue Bing Zheng, Bala Krishna Juluri, Xiaole Mao, Thomas R. Walker, and Tony Jun Huang[a)]

Department of Engineering Science and Mechanics, The Pennsylvania State University, University Park, Pennsylvania 16802, USA

(Received 31 August 2007; accepted 30 October 2007; published online 8 January 2008)

Ordered Au nanodisk arrays were fabricated on glass substrates using nanosphere lithography combined with a two-step reactive ion etching technique. The optical properties of these arrays were investigated both experimentally and theoretically. Specifically, the effects of disk diameter on localized surface plasmon resonance (LSPR) were characterized and compared with results from discrete dipole approximation (DDA) calculations. The effects of glass substrate, Cr interfacial layer, and Au thickness on LSPR were investigated computationally. Furthermore, thermal treatment was found to be essential in improving the nanodisk arrays' LSPR properties. Using atomic force microscopy and DDA calculations, it was established that the improvements in LSPR properties were due to thermally induced morphologic changes. Finally, microfluidic channels were integrated with the annealed disk arrays to study the sensitivity of LSPR to the change in surroundings' refractive index. The dependence of LSPR on surroundings' refractive index was measured and compared with calculated results. © *2008 American Institute of Physics*. [DOI: 10.1063/1.2828146]

I. INTRODUCTION

In recent decades, there has been increasing interest in the plasmonic properties of noble metal nanostructures. These properties are of tremendous importance to nanophotonic devices and circuits.[1–5] In addition, metal nanostructures and their plasmonic properties have been widely used in biomedical applications including biosensing and therapeutics.[6–9] Localized surface plasmon resonance (LSPR) refers to the excitation of surface plasmons by light for nanometer-sized metallic structures.[10] The position and intensity of LSPR are highly sensitive to the size, shape, spacing, and environment of nanostructures.[11–14] This sensitivity has fostered interest in the fabrication of metal nanostructures with different geometries (e.g., rods, rings, prisms, cubes, shells, and rice grains).[15–18] Traditionally, metal nanostructures are prepared by the controlled precipitation and concurrent stabilization of the incipient colloids.[10] Recent advances in preparations of colloids have engendered a variety of methods that enable reproducible generation of monodisperse metal nanoparticles in relatively large quantities.[15] The colloidal nanoparticles have been applied in biosensing, and medical imaging and therapy.[8,9] In comparison with the colloidal nanoparticles in suspensions, ordered metal nanostructures immobilized on substrates are of particular interest for applications such as nanoscale waveguides, surface-enhanced Raman spectroscopy (SERS), and biosensors.[10] The interest on the immobilized nanoparticles arises from several advantages unique to the nanoparticle arrays: easy control of interparticle spacings and positions, and thus the plasmonic properties; no capping agents or stabilizers required in contrast to colloidal nanoparticles, thus ready for various surface functionalizations; and capability for repeated use of the nanoparticles by releasing the absorbed or bounded substances from previous experiments.[10]

The development of cost-effective methods to fabricate the immobilized metal nanostructures presents a significant challenge to the nanoscience and nanotechnology community.[19] The microelectronics industry has established sophisticated infrastructures for patterning nanoscale features by conventional lithography techniques such as photolithography, electron beam lithography, and focused ion beam lithography.[20–24] Although commercially available and widely implemented in manufacturing, these conventional nanofabrication techniques are limited by their high cost, low throughput, and difficulty in accessing the facilities.[21] The limitations of conventional techniques have motivated the development of "unconventional" approaches, such as scanning probe lithography,[25,26] soft lithography,[27,28] and nanoimprinting lithography (NIL).[29,30]

The aforementioned nanofabrication approaches are capable of generating arbitrary patterns with dimensions smaller than 100 nm. Recently, several simpler approaches have been exploited that focus on creating regular patterns of nanostructures such as arrays of holes or pillars.[31–36] In particular, nanosphere lithography (NSL), where a template formed by the self-assembly of monodisperse nanospheres on flat surfaces acts as an etching/deposition mask, is a low-cost, high-throughput method for producing ordered, geometrically tunable nanostructure arrays.[37,38] One disadvantage of the conventional NSL is its limited pattern design. Only triangular- and hexagonal-shaped metal nanoparticles can be produced from deposition through monolayer and double layer of close-packed nanospheres. The LSPR properties of the triangle nanoparticles and their applications in biosensing have been studied intensely.[39] Recently, several methods have been developed to extend the NSL in order to

[a)]Electronic mail: junhuang@psu.edu.

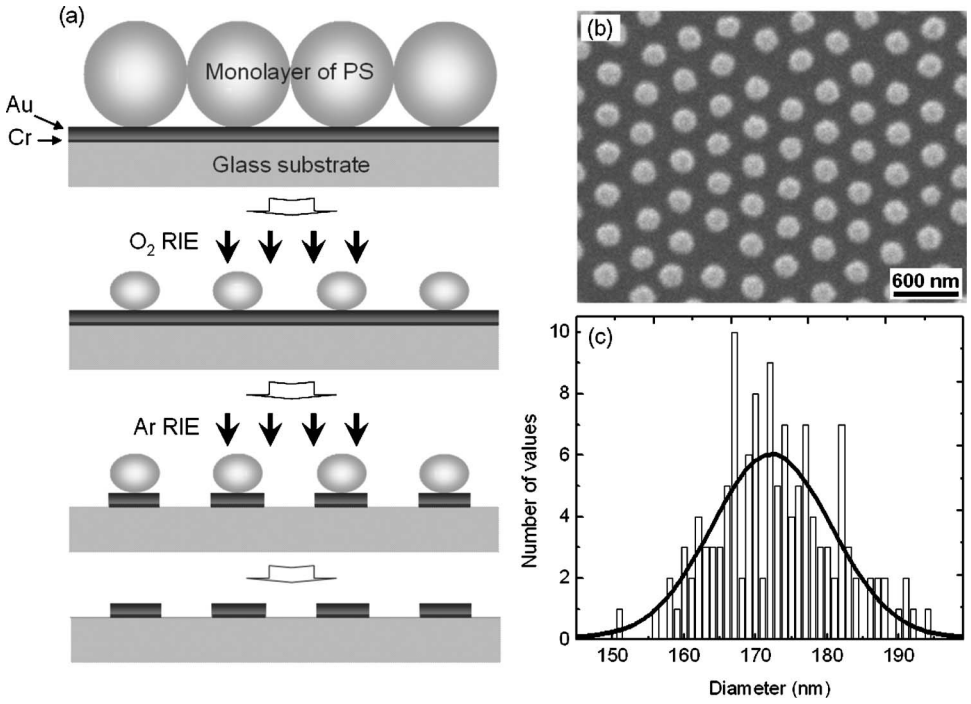

FIG. 1. (a) Schematic of the nanodisk fabrication process. (b) A SEM image of hexagonal-arranged Au disk arrays on a glass substrate. (c) A histogram of disk diameter distribution obtained with an Able Image Analyzer (Mu Laboratories, Slovenia). The black curve represents results from Gaussian fitting.

fabricate nanoparticles of different patterns and shapes.[40] The variety of shapes is especially important for plasmonics, in both fundamental study and applications, due to the shape dependence of LSPR.

Here, we integrated the conventional NSL with two types of reactive ion etching (RIE) processes to produce long-range ordered Au nanodisk arrays. The short-range ordered metal nanodisks have been fabricated on substrates by Ar ion beam etching with randomly deposited nanospheres as masks, and their LSPR properties have been investigated.[41] Compared with the short-range counterparts, the long-range ordered metal nanodisk arrays have better regularity and narrower plasmon resonance bands from the far-field coupling effects among arrays.[42,43] These advantages make them attractive for applications such as SERS and surface plasmon resonance sensors. We investigated the LSPR properties of the long-range ordered Au nanodisk arrays systematically through both experimental and computational methods. Specifically, the effects of various parameters (including disk diameter, Au thickness, glass substrate, and Cr interfacial layer thickness) on LSPR were characterized and compared with results from discrete dipole approximation (DDA) calculations. Furthermore, the LSPR properties of disk arrays were found to be significantly improved by thermal treatment processes. Finally, the effects of surroundings' refractive index on the LSPR of Au nanodisks were measured through a plasmofluidic chip and compared to DDA-calculated results.

II. EXPERIMENTAL DETAILS

Fabrication of long-range ordered Au nanodisk arrays. Ordered Au nanodisk arrays of different sizes were fabricated on glass substrates using NSL combined with two RIE processes [Fig. 1(a)]. First, a Au thin film of controlled thickness (~33 nm) was deposited onto a glass substrate by a thermal evaporation technique. A thin Cr layer (~3 nm) was sandwiched between the Au film and the glass substrates as an adhesive layer. The glass substrate was precleaned by immersion in piranha solution ($H_2SO_4:H_2O_2=3:1$) at 80 °C for 30 min, followed by rinsing with de-ionized (DI) water and drying with N_2 gas. Second, a self-assembled monolayer of close-packed PS nanospheres (320 nm in diameter) was deposited onto the Au surface per the following procedure:[44] (a) The substrate was placed at the bottom of a petri dish filled with DI water. (b) PS nanospheres (10 wt %, Bangs Laboratories) were mixed with the same volume of ethanol. (c) After 200 μl of the mixture was slowly applied to the water surface by a pipette, a monolayer of nanospheres appeared on the water surface. (d) A surfactant, sodium dodecyl sulfate (SDS) of 2% concentration, was used to drive the nanospheres into a hexagonally arranged, close-packed monolayer. (e) The aqueous mixture in the petri dish was drained, causing the monolayer to transfer to the substrate surface.

Third, O_2 RIE and Ar RIE (Plasma-Therm 720) were carried out to morph the closely packed PS nanosphere monolayer into arrays of separated nanoellipses and to selectively etch a portion of the Au and Cr films that was not protected by the nanoellipses. In these two RIE processes, the parameters included 20 SCCM (SCCM stands for Standard Cubic Centimeters per Minute) gas flow, 100 mTorr pressure, and 300 W power density.

Thermal treatment. The disk arrays were annealed in a furnace under ambient atmospheric conditions. All samples were annealed at 500 °C for 4 h, and cooled naturally. The ramp-up rate was set at 25 °C/min.

Fabrication of microfluidic channels. A polydimethylsiloxane (PDMS) microfluidic device with one inlet, one outlet, and a chamber (4×4 mm^2) was fabricated using a standard mold replica technique. The mold was made on a silicon substrate by deep reactive ion etching (DRIE). A posi-

tive photoresist (Shipley 1827) was lithographically patterned on the substrate as mask for DRIE. The substrate was etched to create a mold of approximately 50 μm height. A two-part mixture (Sylgard™ 184 silicone elastomer base and Sylgard™ 184 silicone elastomer curing agent) was mixed at a 10:1 ratio and cast onto the silicon mold, followed by curing at 70 °C for 2 h. After the PDMS was cured, it was peeled from the mold. Inlets and outlets were created by drilling on PDMS with a SiC drill bit. The PDMS was subsequently bonded to the substrate with disk arrays. Polyethylene tubes were inserted into the inlet/outlet holes to connect the chamber to a syringe (BD biosciences) for fluid injection. Prior to each measurement, 500 μl fresh fluid was injected manually to rinse off residue from previously used fluids.

Structural characterizations. SEM images were taken on a Hitachi S-3500N with an accelerating voltage of 5 kV. Atomic force microscopy (AFM) images were taken under ambient conditions using a Digital Instruments Dimension 3100 operated in a tapping mode.

Optical characterizations. The extinction spectra of the arrays were recorded on either a Lambda 950 UV-Vis-NIR spectrophotometer or an HR4000 spectrophotometer from Ocean Optics Inc. An unpolarized incident light beam was normal to the substrate surface. The HR4000 spectrophotometer had a wavelength range of 350–1100 nm, and the Lambda 950 had a wavelength range of 200–2000 nm.

III. RESULTS AND DISCUSSION

A. Structural characterization of nanodisks

Figure 1(b) shows a scanning electron microscopy (SEM) image of hexagonally arranged Au nanodisk arrays on a glass substrate. The arrays' period was 320 nm as determined from the SEM images, which was consistent with the diameter of nanospheres. In the fabrication, O_2 RIE (Plasma-Therm 720) was carried out for 30 s to reduce the diameter of PS nanospheres and produce separated nanoellipses. With the PS nanoellipse arrays as an etching mask, the following Ar RIE step was carried out for 100 s to selectively etch the portion of Au and Cr layers that were not protected by the nanoellipses. Finally, ordered Au arrays were produced on the substrates after removing the remaining PS (with toluene in ultrasonics for 3 min). Figure 1(c) is a histogram of disk diameter distribution obtained with the Able Image Analyzer (Mu labs, Slovenia). The black curve in the inset is from Gaussian fitting, which gives a mean diameter of 172±16 nm for the Au nanodisks.

The mean disk diameter could be tuned by changing the O_2 RIE time. Figure 2 shows the evolution of mean disk diameter with O_2 RIE time. In this case, the Ar RIE was carried out for 200 s. The inset of Fig. 2 shows typical AFM images of nanodisk arrays after different etching times. The mean diameter was obtained based on the AFM images of a larger scanning area (4×4 μm^2) and the Able Image Analyzer. We can see that Au nanodisks with an arbitrary diameter can be obtained by controlling the O_2 RIE time. Longer

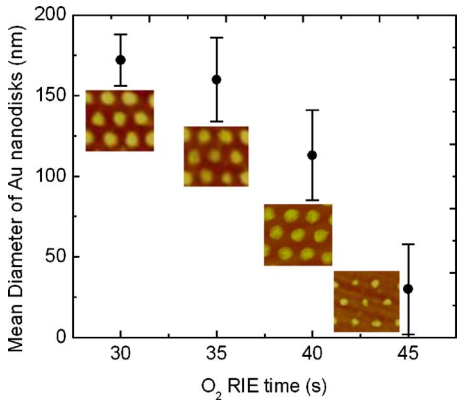

FIG. 2. (Color online) Evolution of mean disk diameter with O_2 RIE time. The inset shows typical AFM images of arrays after different etching times.

RIE times result in smaller disk diameters and broader diameter distributions. Controlling other parameters in the RIE process, such as power, can also tune the disk diameter. In addition, by choosing PS nanospheres of different diameters, the period of nanodisks can also be tuned.

B. Effects of nanodisk diameter on LSPR

The LSPR properties of the Au nanodisk arrays were studied by recording the extinction spectra (absorption +scattering). Figure 3(a) shows the extinction spectra of the nanodisk arrays with different diameters. The Au nanodisks of different diameters were obtained by tuning either the O_2 RIE time or power. The inset in Fig. 3(a) is a schematic of a unit of Au nanodisk arrays, and all the arrays have a period of 320 nm. A Lambda 950 UV-Vis-NIR spectrophotometer was used to record the spectra. The spectra for all the disk arrays with different diameters exhibit broad LSPR bands, which can be identified as the in-plane dipole resonance.[45] The peak position redshifts when the diameter of nanodisks increases. The absorption at the small wavelength range (<400 nm) arises from the substrate.

To further investigate the effects of disk diameter on peak position and bandwidth, DDA calculations were carried out. DDA, developed by Purcell and Pennypacker,[46] is a powerful tool to study the light scattering behavior of particles whose dimensions are close to the wavelength of visible light. It has been applied to both isolated metal nanoparticles and nanoparticle arrays.[47] In this study, we used the open program DDSCAT (version 6.1) by Draine and Flatau[48] to simulate the plasmonic behavior of Au nanodisks. The wavelength-dependent dielectric constants for Au were obtained from Palik.[49] To achieve the DDA simulation results shown in Fig. 3, we assumed that an isolated Au nanodisk was immersed in a homogeneous medium. The disks were 33 nm thick and their diameters ranged from 100 to 270 nm. The incident light was normal to the nanodisks' bases and linearly polarized along +*y* in the "Laboratory Frame."[48] Although this assumption deviates from the experimental conditions, where an unpolarized light source was used, it should introduce little error into the simulation results because of the symmetric geometry of the nanodisks.

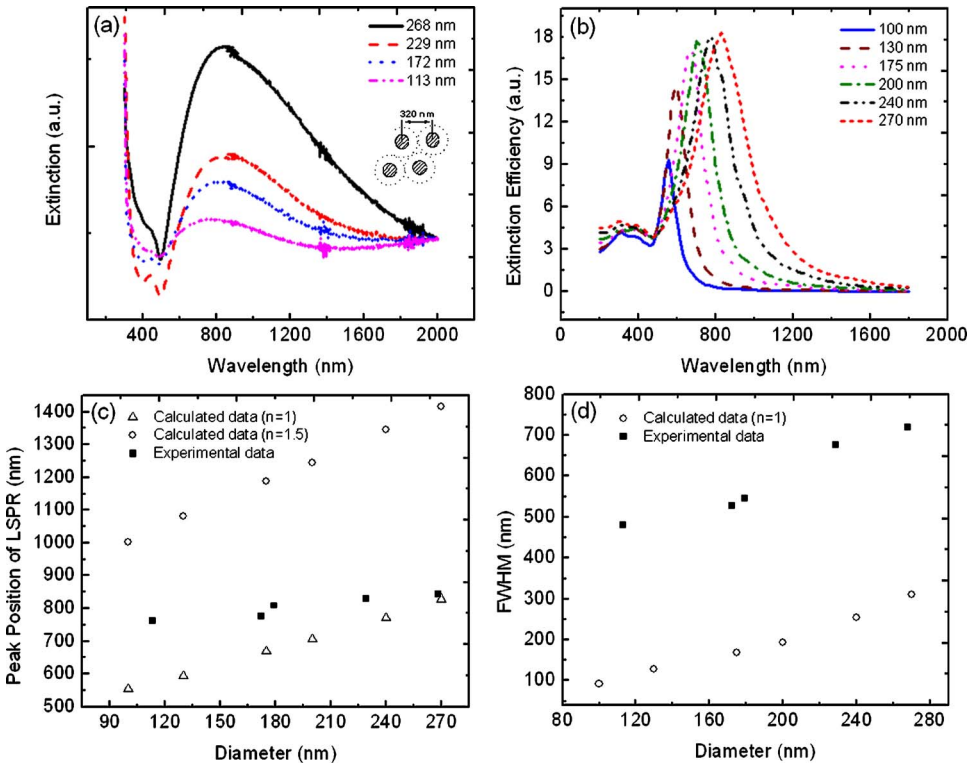

FIG. 3. (Color online) (a) Measured extinction spectra of Au disk arrays with different diameters. The inset is a schematic of a unit of arrays. (b) Calculated extinction efficiency as a function of incident light wavelength for Au disks with different diameters. (c) Evolution of peak position of LSPR band as a function of disk diameter. The squares stand for experimental data, the triangles are calculated data for disks in air ($n=1.0$), and the circles are calculated data for disks in glass ($n=1.5$). (d) Evolution of FWHM of LSPR band as a function of disk diameter. The squares stand for experimental data, and the circles are calculated data for disks in air.

Figure 3(b) shows the calculated extinction efficiency as a function of incident light wavelength. The disks were assumed to be in air ($n=1$). As shown in Fig. 3(b), as the mean disk diameter increases, the peak of the dipole resonance redshifts with higher intensity, a trend consistent with the experimental results [Fig. 3(a)].

To further compare the DDA-calculated results with the experimental data, Figures 3(c) and 3(d) show the evolution of peak position and full width at half maximum (FWHM) as a function of disk diameter. In Fig. 3(c), the two groups of calculated data show similar trend: the peak position increases with disk diameter. At the same disk diameter, the peak position redshifts as the medium is changed from air to glass. Unsurprisingly, the experimental data are distributed between the two groups of calculated results. This is because the bases of nanodisks contact glass substrates ($n=1.5$), and the tops and sidewalls are exposed to air. The refractive index of the media (composed of both air and glass) around the Au nanodisks should be between 1 and 1.5. With the increase of disk diameter, the peak position of experimental LSPR band approaches the calculated values for disks in air. The FWHM of both calculated and experimental spectra increases with disk diameter [Fig. 3(d)]. However, the FWHM of the calculated spectra is much smaller than that of the experimental spectra. The discrepancy between the experimental and computational results arises primarily from imperfect experimental conditions, such as defects, nonuniform disk sizes, and morphology, and deviation of actual thickness of Au disks from that of the original thin films. In addition, the effects of substrate and Cr interfacial layers on the LSPR have not been considered in the current DDA-based model.

C. Effects of substrates and Cr interfacial layers on LSPR

To provide more accurate simulation results, we developed DDA-based models that consider the effects of glass substrate and Cr interfacial layers on LSPR. Three disk configurations were constructed in this investigation. In the first one, a single Au nanodisk (diameter, 100 nm; thickness, 20 nm) was discretized to 10 112 dipoles. In the second one, the same disk was situated on a cylindrical glass substrate (refractive index, 1.5; diameter, 150 nm; thickness, 30 nm); this model took 44 048 dipoles. For the third one, a thin Cr layer (diameter, 100 nm; three different thicknesses, 2.5, 5, and 10 nm) was sandwiched between the Au nanodisk and the glass substrate, yielding 45 312, 46 576, and 49 104 dipoles, respectively. The wavelength-dependent refractive index of Cr was obtained from Palik.[49] The number of dipoles was selected to ensure accurate simulation results.

Figure 4(a) shows the calculated extinction spectra for all the three configurations. The inset in Fig. 4(a) shows the cross-sectional schematics of the models. The glass substrate causes a redshift of the LSPR peak position and lowers the peak intensity. The redshift arises from the increased refractive index of the disks' surroundings; this finding is consistent with the results in Fig. 3(c). Compared with the LSPR of a bare Au nanodisk on a glass substrate, the existence of a Cr interfacial layer significantly weakens LSPR and broadens FWHM. When the thickness of the Cr layer increases, the peak position blueshifts with decreased peak intensity and broadened FWHM. These results indicate that the LSPR properties of Au nanodisks are compromised by the existence of Cr interfacial layer, a component essential for the disks' structural stability on glass substrates. Therefore, the

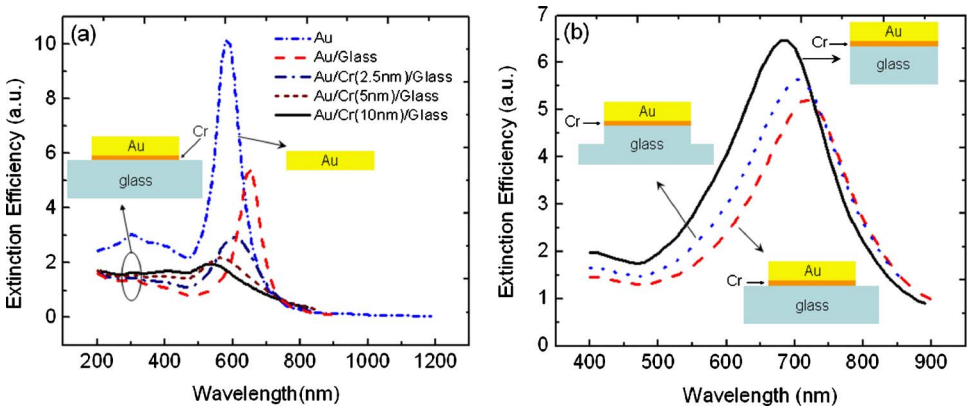

FIG. 4. (Color online) (a) Calculated extinction spectra of Au disks with the following three configurations: Au, Au/glass, Au/Cr/glass. (b) Calculated extinction spectra of Au disks with different substrate configures to investigate the overetching effects. The insets show the cross-sectional schematics of the models.

thickness of Cr interfacial layer should be optimized to balance the needs on both LSPR properties and structural stability.

D. Effects of overetching on LSPR

When longer Ar RIE time is used, glass substrates will be overetched. To investigate the overetching effects on the LSPR of the disks, we constructed three different models in the DDA calculations. The models cover the typical substrate configurations that could be produced in different experimental conditions. In the first model, a Au nanodisk (17 nm in thickness and 140 nm in diameter) with Cr layer (3 nm in thickness and 140 nm in diameter) is situated on a glass substrate (45 nm in thickness and $n=1.52$) of the same diameter. This model simulates a situation in which the substrate is thoroughly overetched. The second model is similar to the first one except that the diameter of glass substrate is increased to 200 nm. This model represents a no-overetching case. The third model simulates a situation in which the substrate is partially overetched. For this purpose, the glass substrate is comprised of two parts: the upper part has a diameter of 140 nm and a thickness of 20 nm, and the lower part has a diameter of 200 nm and a thickness of 25 nm. The calculated results for the three models [Fig. 4(b)] indicate that the overetching of the substrate blueshifts the LSPR peak position with enhanced peak intensity. This blueshift arises from decreased average refractive index of the surroundings during the overetching process.

E. Effects of Au nanodisk thickness on LSPR

By depositing Au thin films of different thicknesses on glass substrates before the lithographic process, nanodisks of different thicknesses can be obtained. The effects of Au nanodisk thickness on LSPR were evaluated based on DDA calculations. In the computational model, the disk diameter was fixed at 175 nm and the Au thickness ranged from 10 to 150 nm. The rest of the calculation conditions were the same as those used in Fig. 3(b). Figure 5(a) shows the calculated extinction efficiency as a function of incident light wavelength. Figure 5(b) depicts the peak position and FWHM of LSPR band as a function of disk thickness. The inset in Fig. 5(b) is a schematic of three disks with different thicknesses. These results indicate that in contrast to Au nanospheres whose LSPR peak positions are reported to be independent of their dimensions without considering retardation effects,[50] Au nanodisks exhibit dimension-dependent LSPR characteristics. Reducing the thickness of the Au nanodisks redshifts the LSPR peak with narrower FWHM and higher peak intensity.

F. Effects of thermal treatment on LSPR

Our prior study showed that thermal treatment of triangular Au nanoparticle arrays lowers the FWHM and increases the peak intensity of the LSPR spectra.[51] These changes are caused by improved morphological uniformity among particles. In this work, similar thermal treatment was applied to improve the LSPR of Au nanodisk arrays. The disks were fabricated on the glass substrate with O_2 RIE of 30 s and Ar RIE of 200 s, and annealed at 500 °C for 4 h.

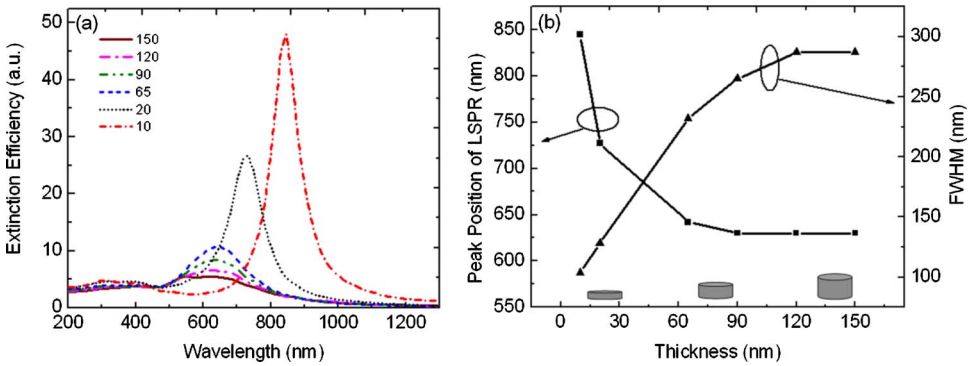

FIG. 5. (Color online) (a) Calculated extinction efficiency as a function of incident light wavelength for disks of different thickness. (b) Evolution of peak position and FWHM of LSPR band as a function of disk thickness. The inset is a schematic of disks with different thicknesses.

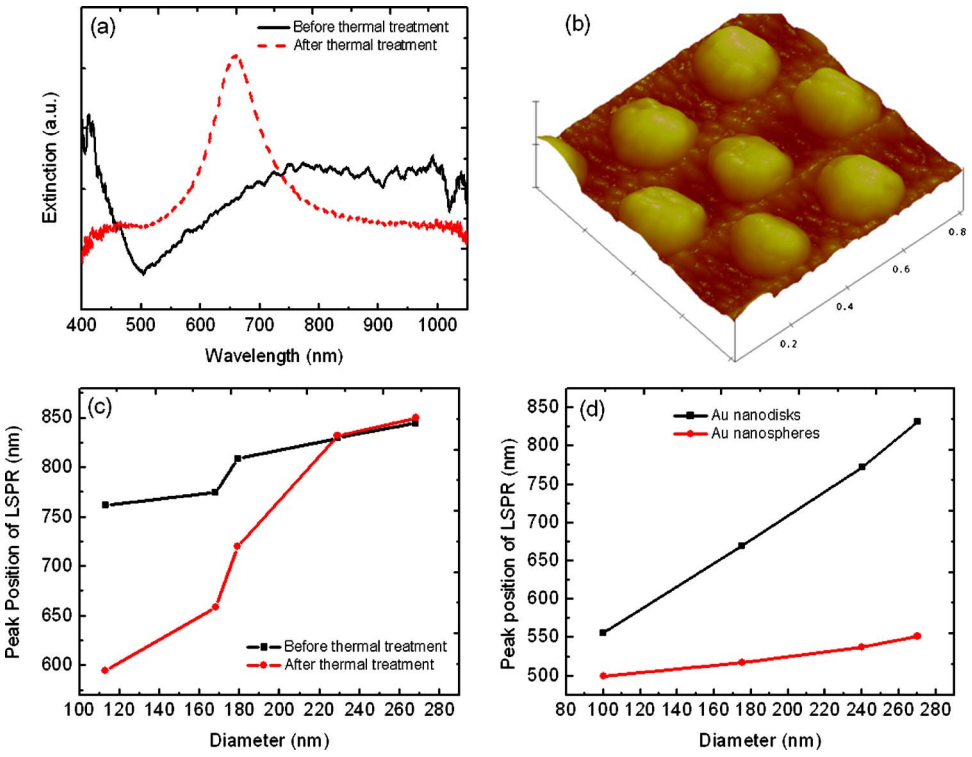

FIG. 6. (Color online) (a) Extinction spectra of disk arrays before and after annealing. (b) a 3D AFM image of annealed disk arrays. (c) Experimental data on the evolution of LSPR peak position, before and after annealing, as a function of disk diameter. (d) Calculated results on the evolution of LSPR peak position as a function of diameter for both nanodisks and nanospheres.

Figure 6(a) shows the extinction spectra of disk arrays before and after the annealing process. The disk array before annealing exhibits a broad LSPR band when characterized by an HR4000 spectrophotometer from Ocean Optics. On the other hand, the annealed disk array shows an intense, narrow LSPR band using the same instrument. Upon the annealing process, the FWHM of the LSPR band decreases from 259 to 96 nm, the peak position blueshifts from 775 to 659 nm, and the peak intensity more than doubles. The dramatic narrowing of FWHM and increasing of peak intensity are believed to arise from the improved morphological uniformity as well as far-field coupling effects among the disk arrays.[43]

Annealed nanodisks were further examined by AFM to reveal how the annealing process would affect the morphology, and thereby the LSPR, of nanodisks. Figure 6(b) shows a three-dimensional (3D) AFM image of the annealed disk arrays. Compared with the AFM image of the preannealed disks, as shown in Fig. 2, the annealed disks have similar shape but decreased diameters and much smoother surface morphology. This is because Au annealed at a high temperature (500 °C in the present trials) exhibits excellent diffusivity, which reduces RIE-induced defects (e.g., pits and redeposited aggregates) among the disks. Fewer defects lead to more uniform morphology and hence better LSPR characteristics.

To further investigate the effects of thermal treatment on LSPR, we recorded the extinction spectra of Au nanodisk arrays of several diameters before and after the annealing process. The peak position of the LSPR, before and after the annealing, was recorded as a function of the diameter of the preannealed disks and shown in Fig. 6(c). For disks with diameters smaller than 200 nm, the peak positions blueshift upon the annealing process. As the disk diameter increases, the shift in peak position gets smaller upon annealing. When the disk diameter is larger than 200 nm, annealing does not introduce obvious peak shift. These results coincide with our AFM images, which show that the annealing process transforms the smaller disks (<200 nm in diameter) into spherical shape, but does not change the shape of larger ones.

We further carried out DDA calculations to study the LSPR of Au disks/spheres and to reveal how annealing-induced changes in Au morphology (from nanodisks to nanospheres) affect LSPR. The Au disks/spheres were assumed to be immersed in air. The equivalent diameters of the spheres were obtained by assuming that the total mass is conserved during the shape-changing process. The extinction efficiency as a function of wavelength is calculated for both nanodisks and nanospheres. Figure 6(d) shows the evolution of LSPR peak position of both nanodisks and nanospheres as a function of the disk diameter. As the diameter increases, the peak position experiences increased blueshifts upon the morphological transformation from nanodisks to nanospheres. The contrast between Figs. 6(c) and 6(d) confirms the observations from the AFM images: smaller disks become spherical upon annealing, while larger ones do not.

G. Effects of surroundings' refractive index on LSPR

The dependence of LSPR on surroundings' refractive index has been exploited in sensors, filters, and displays.[52–56] For many different sensors, the sensitivity is one of the most important parameters.[57–59] In this work, we evaluate the sensitivity of LSPR to the change in surroundings' refractive index by integrating nanodisk arrays with microfluidic channels. Our approach is an example of plasmofluidics, an emerging field that fuses plasmonics and microfluidics[60–63]

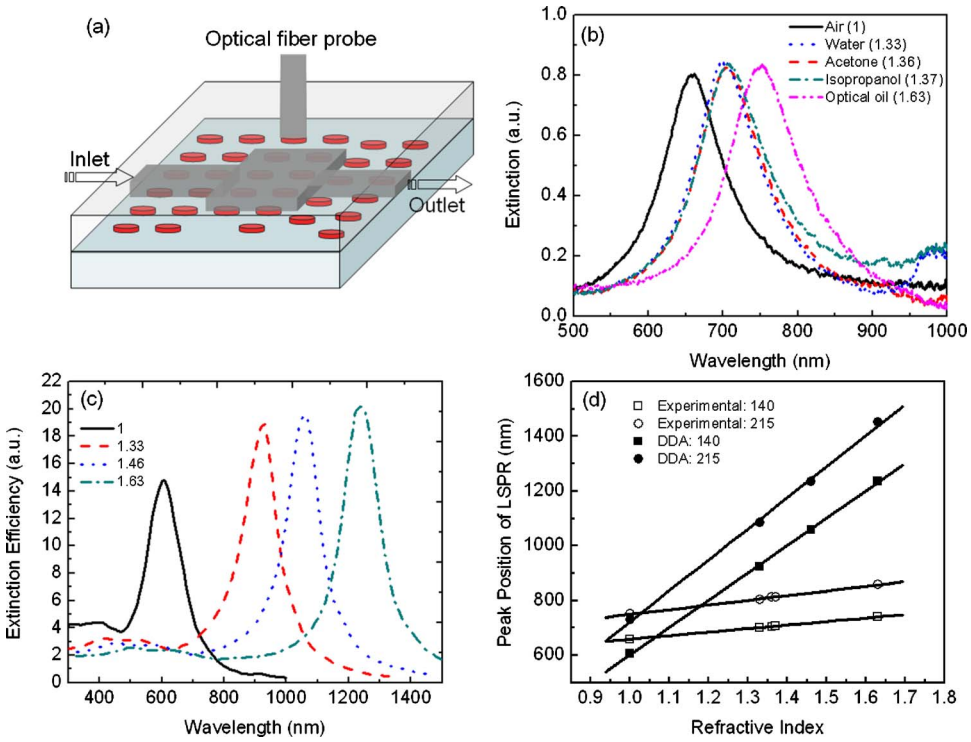

FIG. 7. (Color online) (a) Schematic of a plasmofluidic chip. (b) Extinction spectra recorded from the plasmofluidic chip when exposed to different fluids. (c) Calculated extinction efficiency as a function of wavelength for Au disk embedded in media with different refractive indices. (d) Evolution of LSPR peak position as a function of surroundings' refractive index. The square and circle are for the disks of 140 and 215 nm in diameter, respectively. The open and solid symbols stand for the experimental and DDA calculated data, respectively. The black lines are from linear fitting of the data.

and enables the development of both surface plasmon-based "lab-on-a-chip"[64–67] and fluid-based active plasmonics.[68]

Figure 7(a) is a schematic of a plasmofluidic chip employed in our work. Annealed Au nanodisk arrays on a glass substrate were integrated with a PDMS microfluidic channel. The channel has an inlet, an outlet, and an optical chamber to measure LSPR. Because of its dependence on the surroundings' refractive index, the LSPR of Au nanodisk arrays can be tuned when the microchannel is exposed to fluids of various refractive indices. To handle organic solvents that can attack PDMS, commercial flow cells made of quartz (Starna Cells) were also used in our studies. Two types of annealed Au disks with diameters of ~140 and ~215 nm, respectively, were studied.

Figure 7(b) shows the extinction spectra recorded from the annealed Au nanodisks with diameter of ~140 nm when exposed to different surroundings. The HR4000 spectrophotometer was used to record the spectra. Four fluids with different refractive indices were used: water ($n=1.33$), acetone ($n=1.36$), isopropanol ($n=1.37$), and optical oil ($n=1.63$). The LSPR peak position redshifted and its peak intensity increased when a fluid of higher refractive index was introduced. The observed effects of refractive index on LSPR peak position and intensity [Fig. 7(b)] are consistent with the calculated results [Fig. 7(c)]. In the DDA calculations, the disk diameter and thickness were chosen to be 140 and 33 nm, respectively. Each disk was assumed to be immersed in a homogeneous medium of refractive index ranging from 1 to 1.63. Other parameters used in the simulation were the same as those employed in Fig. 3(b). Figure 7(d) shows the evolution of LSPR peak positions as a function of surroundings' refractive index for two types of disks (diameter, 140 and 215 nm). Both experimental and theoretical results indicate that the LSPR peak position scales linearly with the surrounding refractive index. Based on the slope of the fitted lines, disks of bigger diameter exhibit better sensitivity. The diameter-dependent sensitivity is consistent with analytical results.[69] However, theoretical results show much higher sensitivity than the experimental data. The theoretical and experimental sensitivities for the disks of 140 nm in diameter are 998 and 128 nm/RIU (refractive index unit), respectively. Those for the disks of 215 nm in diameter are 1134 and 171 nm/RIU, respectively.

The discrepancy between experimental and theoretical results can be attributed primarily to three factors. First, in the experiments, only part of the disk (top and sidewalls) was exposed to the surroundings, while in the calculations, the disks were assumed being completely surrounded by the fluidic media. Second, as fluids with different refractive indices passed through the microchannel, residue accumulated on disk surfaces and changed the effective refractive index and thus the LSPR of the disks. Third, during the Ar RIE process, glass substrates were overetched to some degree and the etched materials could be redeposited onto Au disks and reduced the surface areas of Au disks that were exposed to the fluidic media. The contribution from the second factor can be reduced if we functionalize the disk surfaces with a self-assembled monolayer that reduces residue attachment.[70] To reduce the third factor (the redeposition of glass materials on Au disks), Ar RIE conditions should be optimized to minimize the overetching effects.

IV. CONCLUSION

We fabricated long-range ordered Au nanodisk arrays of tunable sizes on glass substrates by combining the conventional NSL with two-step RIE processes, and investigated the LSPR properties of the disks systematically. Both experimental and theoretical studies of the LSPR of the Au nano-

disks indicate that increasing the disk diameter redshifts the peak position and increases the peak intensity as well as the FWHM. Based on the DDA calculations, reducing the thickness of the Au nanodisks redshifts the peak of LSPR with narrower FWHM and higher intensity. Glass substrates cause a redshift of peak position while decreasing the peak intensity. Overetching the glass substrates blueshifts the peak position with increased intensity. On the other hand, the Cr interfacial layer causes a slight blueshift of the peak position while greatly decreasing peak intensity and broadening FWHM. Furthermore, we have found that the annealing process is essential in improving the LSPR properties of Au nanodisks. For disks with diameters smaller than 200 nm, the peak positions blueshift upon the annealing process. When the disk diameter is larger than 200 nm, annealing does not introduce obvious peak shift. These results coincide with the AFM images, which show that the annealing process transforms smaller disks ($<$200 nm) into spherical shape, but does not change the shape of larger ones. The annealed Au disks dramatically narrow the FWHM and increase the peak intensity, which is believed to arise from the improved morphological uniformity as well as far-field coupling effects among the disk arrays. Finally, the sensitivity of LSPR of the annealed disk arrays to the change of surroundings' refractive index was measured through a plasmofluidic chip and compared with DDA calculations.

ACKNOWLEDGMENTS

The authors thank Ashley Colletti for help in preparing the manuscript. This research was supported in part by the start-up fund provided by The Pennsylvania State University and the NSF NIRT grant (ECCS-0609128). Components of this work were conducted at the Penn State node of the NSF-funded National Nanotechnology Infrastructure Network.

[1] H. A. Atwater, S. Maier, A. Polman, J. A. Dionne, and L. Sweatlock, MRS Bull. **30**, 385 (2005).
[2] W. L. Barnes, A. Dereux, and T. W. Ebbesen, Nature (London) **424**, 824 (2003).
[3] N. Fang, H. Lee, C. Sun, and X. Zhang, Science **308**, 534 (2005).
[4] R. Zia, J. A. Schuller, A. Chandran, and M. L. Brongersma, Mater. Today **9**, 20 (2006).
[5] E. Ozbay, Science **311**, 189 (2006).
[6] T. Endo, K. Kerman, N. Nagatani, H. M. Hiepa, D. K. Kim, Y. Yonezawa, K. Nakano, and E. Tamiya, Anal. Chem. **78**, 6465 (2006).
[7] A. J. Haes, L. Chang, W. L. Klein, and R. P. Van Duyne, J. Am. Chem. Soc. **127**, 2264 (2005).
[8] N. L. Rosi, D. A. Giljohann, C. S. Thaxton, A. K. R. Lytton-Jean, M. S. Han, and C. A. Mirkin, Science **312**, 1027 (2006).
[9] C. Loo, A. Lowery, N. Halas, J. West, and R. Drezek, Nano Lett. **5**, 709 (2005).
[10] E. Hutter and J. H. Fendler, Adv. Mater. (Weinheim, Ger.) **16**, 1685 (2004).
[11] W. A. Murray, J. R. Suckling, and W. L. Barnes, Nano Lett. **6**, 1772 (2006).
[12] Y. G. Sun and Y. N. Xia, Science **298**, 2176 (2002).
[13] H. Wang, D. W. Brandl, F. Le, P. Nordlander, and N. J. Halas, Nano Lett. **6**, 827 (2006).
[14] H. Wang, D. W. Brandl, P. Nordlander, and N. J. Halas, Acc. Chem. Res. **40**, 53 (2007).
[15] N. Halas, MRS Bull. **30**, 362 (2005).
[16] C. J. Murphy, T. K. Sau, A. Gole, and C. J. Orendorff, MRS Bull. **30**, 349 (2005).
[17] B. Wiley, Y. G. Sun, J. Y. Chen, H. Cang, Z. Y. Li, X. D. Li, and Y. N. Xia, MRS Bull. **30**, 356 (2005).
[18] Y. N. Xia and N. J. Halas, MRS Bull. **30**, 338 (2005).
[19] Y. N. Xia, J. A. Rogers, K. E. Paul, and G. M. Whitesides, Chem. Rev. (Washington, D.C.) **99**, 1823 (1999).
[20] *Handbook of Microlithography, Micromachining and Microfabrication*, edited by P. Choudhury (SPIE Optical Engineering, Bellingham, WA, 1997).
[21] H. I. Smith and H. G. Craighead, Phys. Today **43**(2), 24 (1990).
[22] D. Brambley, B. Martin, and P. D. Prewett, Adv. Mater. Opt. Electron. **4**, 55 (1994).
[23] F. Cerrina and C. Marrian, MRS Bull. **12**, 56 (1996).
[24] S. A. Maier, M. L. Brongersma, P. G. Kik, S. Meltzer, A. A. G. Requicha, and H. A. Atwater, Adv. Mater. (Weinheim, Ger.) **13**, 1501 (2001).
[25] Y. Kim and C. M. Lieber, Science **257**, 375 (1992).
[26] R. D. Piner, J. Zhu, F. Xu, S. Hong, and C. A. Mirkin, Science **283**, 661 (1999).
[27] Y. N. Xia and G. M. Whitesides, Angew. Chem., Int. Ed. **37**, 550 (1998).
[28] Y. N. Xia and G. M. Whitesides, Annu. Rev. Mater. Sci. **28**, 153 (1998).
[29] S. Y. Chou, P. R. Krauss, and P. J. Renstrom, Appl. Phys. Lett. **67**, 3114 (1995).
[30] S. Y. Chou, P. R. Krauss, and P. J. Renstrom, J. Vac. Sci. Technol. B **14**, 4129 (1996).
[31] N. Kramer, M. Niesten, and C. Schonenberger, Appl. Phys. Lett. **67**, 2989 (1995).
[32] T. Akiba, H. Yoshimura, and K. Namba, Science **252**, 1544 (1991).
[33] A. van Blaaderen, R. Ruel, and P. Wiltzlus, Nature (London) **385**, 321 (1997).
[34] R. C. Furneaux, W. R. Rigby, and A. P. Davidson, Nature (London) **337**, 147 (1989).
[35] C. R. Martin, Acc. Chem. Res. **28**, 61 (1995).
[36] M. Park, C. Harrison, P. M. Chaikin, R. A. Register, and D. H. Adamson, Science **276**, 1401 (1997).
[37] J. C. Hulteen and R. P. Van Duyne, J. Vac. Sci. Technol. A **13**, 1553 (1995).
[38] J. C. Hulteen, D. A. Treichel, M. T. Smith, M. L. Duval, T. R. Jensen, and R. P. Van Duyne, J. Phys. Chem. B **103**, 3854 (1999).
[39] K. A. Willets and R. P. Van Duyne, Annu. Rev. Phys. Chem. **58**, 267 (2007).
[40] Y. B. Zheng, S. J. Wang, A. C. H. Huan, and Y. H. Wang, J. Appl. Phys. **99**, 034308 (2006).
[41] P. Hanarp, M. Käll, and D. S. Sutherland, J. Phys. Chem. B **107**, 5768 (2003).
[42] L. D. Qin, S. L. Zou, C. Xue, A. Atkinson, G. C. Schatz, and C. A. Mirkin, Proc. Natl. Acad. Sci. U.S.A. **103**, 13300 (2006).
[43] L. L. Zhao, K. L. Kelly, and G. C. Schatz, J. Phys. Chem. B **107**, 7343 (2003).
[44] D. F. Liu, Y. J. Xiang, X. C. Wu, Z. X. Zhang, L. F. Liu, L. Song, X. W. Zhao, S. D. Luo, M. J. Ma, J. Shen, W. Y. Zhou, G. Wang, C. Y. Wang, and S. S. Xie, Nano Lett. **6**, 2375 (2006).
[45] A. Brioude and M. P. Pileni, J. Phys. Chem. B **109**, 23371 (2005).
[46] E. H. Purcell and C. R. Pennypacker, Astrophys. J. **186**, 705 (1973).
[47] W. H. Yang, G. C. Schatz, and R. P. Vanduyne, J. Chem. Phys. **103**, 869 (1995).
[48] B. T. Draine and P. J. Flatau, User Guide to the Discrete Dipole Approximation Code DDSCAT 6.1, http://arxiv.org/abs/astro-ph/0409262v2, 2004.
[49] *Handbook of Optical Constants of Solids*, edited by E. D. Palik (Academic, New York, 1985).
[50] *Optical Properties of Metal Clusters*, edited by U. Kreibig and M. Vollmer (Spinger-Verlag, Berlin, 1995).
[51] Y. B. Zheng, T. J. Huang, A. Y. Desai, S. J. Wang, L. K. Tan, H. Gao, and A. C. H. Huan, Appl. Phys. Lett. **90**, 183117 (2007).
[52] T. W. Ebbesen, H. J. Lezec, H. F. Ghaemi, T. Thio, and P. A. Wolff, Nature (London) **391**, 667 (1998).
[53] A. V. Whitney, J. W. Elam, S. L. Zou, A. V. Zinovev, P. C. Stair, G. C. Schatz, and R. P. Van Duyne, J. Phys. Chem. B **109**, 20522 (2005).
[54] D. K. Kim, K. Kerman, M. Saito, R. R. Sathuluri, T. Endo, S. Yamamura, Y. S. Kwon, and E. Tamiya, Anal. Chem. **79**, 1855 (2007).
[55] G. L. Liu, Y. D. Yin, S. Kunchakarra, B. Mukherjee, D. Gerion, S. D. Jett, D. G. Bear, J. W. Gray, A. P. Alivisatos, L. P. Lee, and F. F. Chen, Nat. Nanotechnol. **1**, 47 (2006).
[56] D. A. Stuart, A. J. Haes, C. R. Yonzon, E. M. Hicks, and R. P. Van Duyne, IEE Proc.: Nanobiotechnol. **152**, 13 (2005).
[57] T. J. Huang, M. Liu, L. D. Knight, W. W. Grody, J. F. Miller, and C. M. Ho, Nucleic Acids Res. **30**, e55 (2002).
[58] J. J. Shi, V. K. S. Hsiao, and T. J. Huang, Nanotechnology **18**, 465501

(2007).
[59]V. K. S. Hsiao, J. R. Waldeisen, Y. B. Zheng, P. F. Lloyd, T. J. Bunning, and T. J. Huang, J. Mater. Chem. **17**, 4896 (2007).
[60]S. Takayama, E. Ostuni, P. LeDuc, K. Naruse, D. E. Ingber, and G. M. Whitesides, Nature (London) **411**, 1016 (2001).
[61]Y. B. Zheng, B. K. Juluri, and T. J. Huang, Nanotechnology **18**, 275706 (2007).
[62]X. L. Mao, J. R. Waldeisen, B. K. Juluri, and T. J. Huang, Lab Chip **7**, 1303 (2007).
[63]X. L. Mao, J. R. Waldeisen, and T. J. Huang, Lab Chip **7**, 1260 (2007).
[64]R. Kurita, Y. Yokota, Y. Sato, F. Mizutani, and O. Niwa, Anal. Chem. **78**, 5525 (2006).
[65]Y. Fainman, K. Tetz, R. Rostislav, and L. Pang, Opt. Photonics News **17**, 24 (2006).
[66]X. Heng, D. Erickson, L. R. Baugh, Z. Yaqoob, P. W. Sternberg, D. Psaltis, and C. H. Yang, Lab Chip **6**, 1274 (2006).
[67]G. L. Liu, J. Kim, Y. Lu, and L. P. Lee, Nat. Mater. **5**, 27 (2006).
[68]A. V. Krasavin and N. I. Zheludev, Appl. Phys. Lett. **84**, 1416 (2004).
[69]E. M. Larsson, J. Alegret, M. Käll, and D. S. Sutherland, Nano Lett. **7**, 1256 (2007).
[70]F. Mugele and J. C. Baret, J. Phys.: Condens. Matter **17**, R705 (2005).